International Journal of Solids and Structures 48 (2011) 817–827

Contents lists available at ScienceDirect

International Journal of Solids and Structures

journal homepage: www.elsevier.com/locate/ijsolstr

Constitutive modeling of ice in the high strain rate regime

Trisha Sain *, R. Narasimhan

Technical University of Catalunya, Campus Nord, C1-101 Barcelona, Spain
Department of Mechanical Engineering, Indian Institute of Science, Bangalore 560 012, India

ARTICLE INFO

Article history:
Received 19 April 2010
Received in revised form 12 November 2010
Available online 19 November 2010

Keywords:
Continuum damage mechanics
Brittle damage
Pressure sensitive
Ice

ABSTRACT

The objective of the present work is to propose a constitutive model for ice by considering the influence of important parameters such as strain rate dependence and pressure sensitivity on the response of the material. In this regard, the constitutive model proposed by Carney et al. (2006) is considered as a starting basis and subsequently modified to incorporate the effect of brittle cracking within a continuum damage mechanics framework. The damage is taken to occur in the form of distributed cracking within the material during impact which is consistent with experimental observations. At the point of failure, the material is assumed to be fluid-like with deviatoric stress almost dropping down to zero. The constitutive model is implemented in a general purpose finite element code using an explicit formulation. Several single element tests under uniaxial tension and compression, as well as biaxial loading are conducted in order to understand the performance of the model. Few large size simulations are also performed to understand the capability of the model to predict brittle damage evolution in un-notched and notched three point bend specimens. The proposed model predicts lower strength under tensile loading as compared to compressive loading which is in tune with experimental observations. Further the model also asserts the strain rate dependency of the strength behavior under both compressive as well as tensile loading, which also corroborates well with experimental results.

1. Introduction

Damage produced by ice due to impact upon structural components is a common phenomenon in aerospace industries. It can be considered as a realistic threat to components such as aircraft fuselage and wing skins, leading edge and control surfaces, engine nacelles and fan blades. The damage caused by the potential impact of various type of debris (referred to as foreign object damage or FOD) is always a serious concern for the safe operation of space shuttles. In this regard, the Columbia Space Shuttle tragedy further motivated a large scale safety review of the requirements for certifying the ability of the leading edge of the wing to safely FOD (Columbia Accident Investigation Board, 2003). Given the wide range of debris, impact locations and velocities, a complete experimental test program would be prohibitively expensive and cannot be accomplished in a timely manner. Therefore, finite element analyses need to be performed carefully to simulate the real damage scenario by modeling the projectile and the target realistically. This motivates the development of constitutive models for common foreign objects such as foams, ice, hailstones, etc. However, ice is not a common structural material and commercial finite element codes do not have any appropriate models for it. Further, aside from the interest of aerospace industry, it is rarely subjected to high strain rate impact conditions.

In general, in available literature, ice is regarded as a class of materials rather than a single specific material with well defined properties. It is found in 13 different crystal structures and two amorphous states. There is a large body of existing work that describes the compressive and tensile behavior of ice and its fracture properties in various strain rate regimes, such as Currier and Schulson (1982), Dempsey et al. (1999), Haynes (1978), Kim and Kedward (2000), Schulson et al. (2005). However most of the studies have focused on the mechanical behavior in the creep and quasi-static regimes. A comprehensive review of mechanical behavior of ice including its failure mechanisms, response under different strain rates and fracture properties has been conducted by Schulson (2001). According to him, the sample compressive strengths of ice have been reported to be 14.8 ± 2.3 MPa in its single crystal form at −10 °C. It has been observed from experiments, that fundamental properties of ice such as strength, elastic modulus, Poisson's ratio are functions of temperature, grain size, and most importantly the strain rate (Epifanov, 2005; Petrovic, 2003; Schulson, 2001). At −10 °C, Young's modulus of ice has been reported in the range of 9.7–11.2 GPa and Poisson's ratio in the range 0.29–0.32 (Gold, 1988). In terms of tensile strength, a wide scatter has been observed from 0.7 to 3.1 MPa over a temperature

* Corresponding author at: Technical University of Catalunya, Campus Nord, C1-101 Barcelona, Spain.
E-mail address: tsain@cimne.upc.edu (T. Sain).

0020-7683/$ - see front matter © 2010 Elsevier Ltd. All rights reserved.
doi:10.1016/j.ijsolstr.2010.11.016

range of −10 °C to −20 °C (Petrovic, 2003). It is also found that under both compressive and tensile loading ice generally displays ductile behavior at lower strain rate, but brittle behavior at higher strain rate. Schulson (2001) has reported a dramatic increase in the compressive failure stress of polycrystalline ice from 0.5 MPa to 10 MPa as the strain rate changes from 10^{-8}/s to 10^{-3}/s.

At higher strain rates, relatively few efforts have been made to predict the behavior of ice. To name a few, Jones (1997), Dutta et al. (2003) have considered strain rates in the range from 10–100/s. However the results are counterintuitive, at least based on the understanding of the common engineering materials. The studies by Dutta (1993) and Dutta et al. (2003) suggest that the strength of ice at high strain rate (between 10^2 and 10^3/s) is lower than that obtained in the quasi-static deformation regime. In an early work by Carter (1972), similar trend was reported in compressive strength behavior of ice at higher strain rate. He explained such decrease in compressive strength as a consequence of the inability of ice to deform plastically at high strain rate regime. The study by Jones (1997), however shows the completely opposite trend in the behavior of ice with increasing strain rates. In a recent study, Kim and Keune (2007) used the split Hopkinson pressure bar to study the peak strength of ice in the strain rate range 400–2600/s. The compressive strength of ice was observed to be essentially constant at a level of 19.7 MPa. In a similar investigation, Shazly et al. (2005) used thin samples of ice in a Hopkinson bar to study the effect of strain rate on the dynamic material response of ice. Their experimental results showed that the strength of ice increases with strain rates. The study on the high-strain rate behavior of ice has been extended by Shazly et al. (2009) for a wide range of strain rates considering different crystalline structures of ice. They observed that the peak stress in the specimens are in the range of 20–24 MPa, when the applied strain rate is in the range of 90–460/s. These peak strength levels are markedly higher when compared to those reported in literature for ice under quasi-static deformation conditions (Schulson, 2001).

In an early work, an experimental investigation was conducted by Mcnaughtan and Chisman (1969), to study the effects of impact velocity up to 2500 ft/s, impact angle, plate material properties and thickness on the damage to flat, light alloy plates caused by the impact of one inch diameter hail.

The literature for modeling high velocity ice impacts is even smaller, which is not too surprising considering the availability of efficient and fast computational power only recently and the market for this research is a narrow segment of the aerospace industry. Anghileri et al. (2005) have developed three numerical models of hailstone, using Lagrangian finite element, arbitrary Lagrangian Eulerian, and smooth particle hydrodynamics methods which are available in the general purpose finite element code LS-DYNA. The relative advantages and disadvantages of these methods were assessed and it was concluded that the smoothed particle hydrodynamics model is the most efficient and effective for the analysis of the event. In their study, ice had been modeled as an elastic–plastic material with failure (using the material model referred to as *MAT13 in LS-DYNA). This model allows a plastic hardening behavior that adequately produces the effect of the propagation of the microcracks inside the ice before it crushes, reaching a fluid-like state. When the plastic failure strain is reached all shear stress components are relaxed to zero. Furthermore, if the tensile failure pressure is reached, the material carries only hydrostatic compressive stresses like a fluid.

Pereira et al. (2006) conducted experiments to measure the forces generated by ice projectiles of different crystalline structures impacting a rigid component at various velocities and orientations. It was observed that when the impact velocity is significantly lower than the wave propagation speed, from a visual perspective, the ice projectile acts like an agglomeration of many tiny particles rather than a single solid. The results indicated (for the considered impact velocity range) that the crystalline structure of the ice has negligible effects on the forces generated during impact. In a very recent work, Sherburn and Horstemeyer (2010) reported a study on impact cratering of ice using CTH model. Their study showed a correlation between the damaged volume of the ice crater with the momentum of the aluminum projectile. In their numerical modeling of ice, an equation of state of the Mie–Gruniesen type was developed and Bammann–Cheisa–Johnson plasticity-damage model is used.

Attempts to use existing models, including some intended for brittle materials, demonstrated the need for a physically motivated damage mechanics based model. This provides the impetus for the present study to develop such a constitutive model for ice, which is capable of depicting its response in the impact regime, incorporating the effects of strain rate, pressure sensitivity and other influencing parameters. Moreover, impact experiments show profuse brittle cracking throughout the ice projectiles during impact (Kim and Kedward, 2000). In order to represent this behavior, the proposed constitutive model is further refined to include the progressive damage phenomenon in ice through a continuum damage mechanics approach, based on brittle cracking.

The most relevant work with respect to the present investigation was performed by Carney et al. (2006). They developed a phenomenological model for ice, and performed numerical simulations for impact problems which were compared with experimental results. The critical aspects of the model are the independent failure stress in tension and compression, strain rate sensitivity of the flow stress, ability of the failed ice to continue to carry hydrostatic stress. Along with the conventional elastic–plastic response, a failure model was introduced by them. The final stress was computed as:

$$\sigma = d^e \cdot d^p \cdot (\sigma' - PI), \tag{1}$$

where $d^{\mathbf{e}}$ and $d^{\mathbf{p}}$ are the damage variables associated with the failure due to plastic strain and pressure, respectively. The failure criterion for plastic strain is,

$$d^e = \begin{cases} 0 & \text{if } \overline{\epsilon^p} > \overline{\epsilon^p_{fail}}, \\ 1 & \text{otherwise}, \end{cases} \tag{2}$$

and for pressure it is taken as,

$$d^p = \begin{cases} 0 & \text{if } P > P_{cut\text{-}off} \text{ or } P < P^T_{fail}, \\ 1 & \text{otherwise}. \end{cases} \tag{3}$$

The impact force history obtained from numerical simulations through LS-DYNA was in good agreement with the experimental results. However, the damage model, proposed by Carney et al. (2006) has a serious drawback, since it does not incorporate any damage evolution law. The damage parameters in their model can assume only two limiting values of 0 and 1. Further, a sudden change in value of $d^{\mathbf{e}}$ or $d^{\mathbf{p}}$ from unity to zero, may induce spurious oscillations in the stress response.

Based on the pertinent literature as discussed above, in the present work a constitutive model for ice is developed, which is valid in the high strain rate regime, by considering the phenomenological model proposed by Carney et al. (2006) as a starting basis. An isotropic elastic–plastic material model with progressive damage evolution in the form of brittle cracking is suggested. The elastic response is calculated by considering a split in the strain energy density function into deviatoric and volumetric parts as proposed by Simo and Hughes (1996). The pressure is computed by using the equation of state proposed by Carney et al. (2006), which takes into account the experimental data on pressure versus volumetric strain. The failure stress of ice is taken to be pressure and

strain rate dependent. It should be recalled that the compressive strength for ice more or less lies within the range 5–25 MPa (with a mean value of 15 MPa) over the strain rate 10^{-8}–10^{-2}/s (Petrovic, 2003); whereas the available data for tensile strength shows a wide scatter from 0.7 to 3.1 MPa with a mean value of 1.43 MPa. However it is worth mentioning that the strength of ice largely depends on the grain size and the strain rate. It is also observed that the difference between the tensile strength and compressive strength reduces in the high strain rate regime (tensile strength being 1/4th or 1/5th of the compressive strength), as mentioned in Shazly et al. (2009).

The proposed model is further refined to include brittle damage response of the ice projectiles based on continuum damage mechanics principles. The damage model proposed for brittle materials by Camacho and Ortiz (1996) is followed and modified to take into account inelastic response. The model is based on the hypothesis of strain energy equivalence. Once the damage commences in the material, only the deviatoric part of the strain energy is modified due to damage, keeping the volumetric energy unperturbed. This results in degradation of shear stress. The plastic potential is also modified due to damage, and the plastic flow rule is essentially written in terms of the entire aggregate material. The proposed analytical model is implemented in the general purpose finite element code FEAP (Zienkiewicz and Taylor, 1991) within an explicit solution framework and several numerical examples are solved.

2. Constitutive model for ice

In the present work, the constitutive theory to model the behavior of ice, which was proposed by Carney et al. (2006) is adopted as mentioned in Section 1. A simple isotropic elastic–plastic model with failure was suggested in Carney et al. (2006). The elastic response was represented by considering hypoelastic constitutive theory and the plastic response by following the J_2 flow theory.

However, in the present work, a hyperelastic model is assumed to make the deformation behavior thermodynamically consistent. A multiplicative kinematics is used for elastic–plastic deformation gradient along with the assumption, that the elastic response can be assumed to be linear (Lee, 1969; Lubliner, 1990; Mandel, 1973). Let $\varphi(B)$ represent the time dependent mapping of the reference placement B to the current placement Ω. A multiplicative decomposition of total deformation gradient into elastic and plastic parts is assumed, so that,

$$\mathbf{F} = \nabla_{\mathbf{X}}\varphi = \mathbf{F^e}\mathbf{F^p}. \tag{4}$$

An essential feature of this description is the introduction of an intermediate local configuration, relative to which the elastic response is characterized. A free energy function (stored energy density per unit reference volume) is considered as,

$$\psi = \hat{\psi}(\mathbf{F^e}, \alpha), \tag{5}$$

where α is the set of strain-like internal variables. Throughout the formulation of the governing equations, the stress–strain response is assumed to be isotropic. Accordingly, the free energy is independent of the orientation of the reference configuration. From the second law of thermodynamics (Clausius–Plank inequality), it follows that the rate of dissipated energy density (or, simply, the dissipation) per unit reference volume (Armero, 2004) should be non-negative, so that

$$D = \tau : \mathbf{d} - \dot{\psi} \geqslant 0, \tag{6}$$

where τ and $\mathbf{d}$ are the Kirchoff stress tensor and the rate of deformation tensor, respectively. Without going into the detailed derivation, directly by using the Coleman–Noll argument (i.e., $D = 0$ for an elastic process), one obtains,

$$\tau = \mathbf{2}\frac{\partial\tilde{\psi}}{\partial\mathbf{b^e}}\mathbf{b^e}. \tag{7}$$

Here it is noted that the requirement of isotropy necessitates that the free energy function may be expressed as $\tilde{\psi}(\mathbf{b^e}, \alpha)$, where $\mathbf{b^e} = \mathbf{F^e}\mathbf{F^{eT}}$ is the elastic left Cauchy–Green deformation tensor. For an inelastic process, the dissipation becomes,

$$D = \tau : \mathbf{d^p} + \mathbf{q}\dot{\alpha} \geqslant \mathbf{0}. \tag{8}$$

where $q = -\partial\tilde{\psi}/\partial\alpha$ are the stress like hardening variables and $\mathbf{d^p}$ is the plastic part of $\mathbf{d}$. The plastic flow is assumed to be isochoric so that:

$$\det\mathbf{F^p} = \det\mathbf{C^p} = \mathbf{1}, \tag{9}$$

which implies that,

$$J = \det\mathbf{F} = \det\mathbf{F^e}. \tag{10}$$

2.1. Elastic response

Following the approach adopted by Simo (1988), and consistent with the assumption of isotropy and the notion of an intermediate stress-free configuration, the stress–elastic strain response is characterized by a stored-energy function of the form:

$$\psi = U(J^e) + \overline{W}(\bar{\mathbf{b}}^{\mathbf{e}}). \tag{11}$$

Here, $U(J^{\mathbf{e}})$ and $\overline{W}(\bar{\mathbf{b}}^{\mathbf{e}})$ are the volumetric and deviatoric parts of ψ respectively, where $\bar{\mathbf{b}}^{\mathbf{e}}$ (in order to make it volume preserving) is given by,

$$\bar{\mathbf{b}}^{\mathbf{e}} = J^{e-2/3}\mathbf{b^e} = J^{\mathbf{e}-2/3}\mathbf{F^e}\mathbf{F^{eT}}. \tag{12}$$

The explicit forms of the above terms and subsequent derivation of Kirchoff stress tensor are reported in Simo and Hughes (1996) and hence omitted here. The final expression for Kirchhoff stress tensor for a material obeying Hooke's law can be written as follows:

$$\tau = -\mathbf{p1} + \tau' = \frac{\kappa}{\mathbf{2}}(\mathbf{J^{e^2}} - 1) + \mu\mathbf{dev}[\bar{\mathbf{b}}^{\mathbf{e}}], \tag{13}$$

where (p) and (τ') are the pressure and deviatoric components respectively. For ice, certain modifications were suggested by Carney et al. (2006). In particular, a specific equation of state relating the pressure to volumetric strain is assumed based on experimental results under compressive loading. The experimental pressure–volumetric strain curves depicting both loading and unloading as reported in Carney et al. (2006), are shown in Fig. 1. Based on this figure, an empirical equation relating the (Cauchy) pressure component P with the volumetric strain measure (ϵ_V) is written as,

$$P = \hat{C}(\epsilon_V) + \gamma\hat{T}(\epsilon_V)E, \tag{14}$$

where $\epsilon_V = \ln(J)$. Here, E the internal energy per reference volume, $\hat{C}$ and $\hat{T}$ are tabular functions and γ is the Gruneisen coefficient. In the present calculations, γ is taken as zero following Carney et al. (2006). Hence, the second term vanishes. From Fig. 1, it is seen that the pressure remains constant at a value of 68.95 MPa as soon as $\epsilon_V = 0.008$ and unloading occurs linearly. In the present study, an equation is fitted to the experimental curve as given by,

$$\begin{aligned} P(\text{MPa}) &= 1.7232\times10^5\epsilon_V^2 - 0.0738\times10^5\epsilon_V, \quad \text{for } \epsilon_V < 0.008,\\ &= 68.95, \quad \text{for } \epsilon_V \geqslant 0.008. \end{aligned} \tag{15}$$

Due to the lack of tension test data, the same relation between pressure and volumetric strain is assumed in the present study, with an opposite sign as,

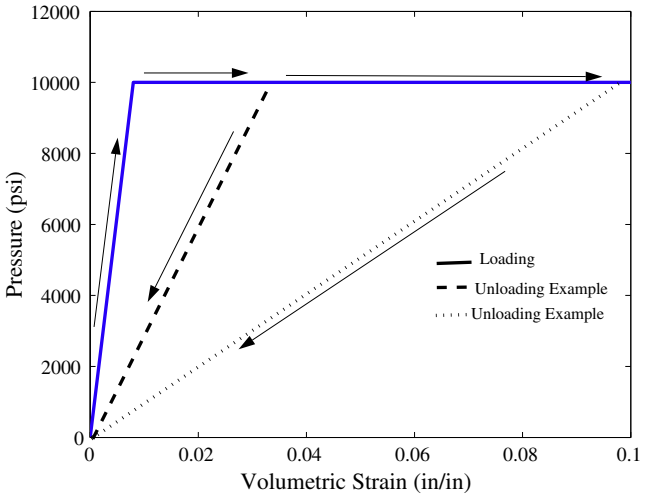

Fig. 1. Pressure versus volumetric strain with loading and unloading (Carney et al., 2006).

$$P(\text{MPa}) = -1.7232 \times 10^5 \epsilon_V^2 - 0.0738 \times 10^5 \epsilon_V, \quad \text{for } \epsilon_V < 0.008$$
$$= -68.95, \quad \text{for } \epsilon_V \geqslant 0.008. \tag{16}$$

2.2. Plastic response

In order to describe the plastic behavior of ice, a plastic flow rule based on the current configuration is used. It is assumed that plastic spin $\mathbf{w^p} = \mathbf{0}$ and hence $\mathbf{l^p} = \mathbf{d^p}$, (where $\mathbf{d^p}$ is the plastic rate of deformation). For a material obeying J_2 flow theory, $\mathbf{l^p}$ can be written as:

$$\mathbf{l^p} = \mathbf{F^e}\dot{\mathbf{F}}^{\mathbf{p}}(\mathbf{F}^{\mathbf{p}-1}\mathbf{F}^{\mathbf{e}-1}) = \dot{\gamma}^{\mathbf{p}}\bar{\mathbf{r}}, \tag{17}$$

where $\bar{\mathbf{r}}$ is the plastic flow direction and $\dot{\gamma}^{\mathbf{p}}$ is an effective visco-plastic strain rate. In the case of J_2 flow theory, $\bar{\mathbf{r}}$ is given by:

$$\bar{\mathbf{r}} = \frac{3}{2}\frac{\sigma'}{\bar{\sigma}}, \tag{18}$$

where σ is the Cauchy stress tensor. The effective Mises stress is defined as:

$$\bar{\sigma} = \left[\frac{3}{2}\sigma_{ij}\prime\sigma'_{ij}\right]^{\frac{1}{2}}, \tag{19}$$

where, the deviatoric component of Cauchy stress σ'_{ij} is given by,

$$\sigma'_{ij} = \sigma_{ij} - \mathbf{P}\delta_{ij}, \tag{20}$$

with $P = -\sigma_{kk}/3$, denoting the pressure.

The next important step in plastic deformation is to formulate an evolution equation for visco-plastic parameter $\dot{\gamma}^{\mathbf{p}}$, specific for ice. According to Carney et al. (2006), the flow stress evolves following the relation given as:

$$\sigma_y = \hat{S}(|\mathbf{d^p}|, \mathbf{P})\hat{\sigma}_{\mathbf{f}}(\bar{\epsilon}^{\mathbf{p}}). \tag{21}$$

The scaling function, $\hat{S}$, is composed of two tabular functions of the strain rate at a specified pressure P, and it is interpolated between them for any other computed pressure as:

$$\hat{S}(|\mathbf{d^p}|, \mathbf{P}) = \mathbf{f}\hat{\mathbf{C}}_{\mathbf{C}}(|\mathbf{d^p}|) + (\mathbf{1} - \mathbf{f})\hat{\mathbf{C}}_{\mathbf{T}}(|\mathbf{d^p}|). \tag{22}$$

The function f is given by

$$f = \min\left[1, \max\left(0, \frac{P - P_T}{P_C - P_T}\right)\right], \tag{23}$$

where C and T denote compression and tension, respectively, and $\hat{C}_C$, $\hat{C}_T$ are tabular functions of strain rate at constant pressure P_C and P_T, respectively. Carney et al. (2006) reported the experimental data for $\hat{C}_C$, whereas the tension data was unavailable.

In the present study, in order to simulate the relation between tensile and compressive yield stress which is $\sigma_0\rfloor_T \approx \sigma_0\rfloor_C/10$ (see Petrovic, 2003; Shazly et al., 2005), it is assumed that $[\hat{C}_T = \hat{C}_C/10]$. On using this assumption, Eq. (22) can be rewritten as:

$$\hat{S}(|\mathbf{d^p}|, \mathbf{P}) = \left(\frac{\mathbf{9f + 1}}{\mathbf{10}}\right)\hat{\mathbf{C}}_{\mathbf{C}}(|\mathbf{d^p}|) = k\hat{\mathbf{C}}_{\mathbf{C}}(|\mathbf{d^p}|), \tag{24}$$

where $k = (9f + 1)/10$ is a new variable introduced to simplify the expression. In order to evaluate the function f according to Eq. (23), two extreme loading condition can be considered. In case of uniaxial tension f is zero, while $f = 1$ under uniaxial compressive loading. Hence, one can obtain two values of k for these two loading conditions as:

$$k = \frac{1}{10}, \quad \text{for } f = 0, \quad \text{and}$$
$$k = 1, \quad \text{for } f = 1. \tag{25}$$

In the above equations, the norm of $|\mathbf{d^p}|$ is defined as:

$$|\mathbf{d^p}| = \sqrt{\frac{\mathbf{2}}{\mathbf{3}}(\mathbf{d^p} : \mathbf{d^p})}. \tag{26}$$

For J_2 flow theory, it turns out that, $|\mathbf{d^p}| = \dot{\gamma}^{\mathbf{p}}$.

Assuming isotropic hardening, $\hat{\sigma}_f$ in Eq. (21) is given as:

$$\hat{\sigma}_f(\bar{\epsilon}^p) = \sigma_0 + h\bar{\epsilon}^p, \tag{27}$$

where σ_0, h and $\bar{\epsilon}^p$ are initial yield stress under uniaxial compression, hardening modulus and equivalent plastic strain, respectively. The Mises equivalent plastic strain is defined as:

$$\bar{\epsilon}^p = \int_0^t \sqrt{\frac{2}{3}(\mathbf{d^p} : \mathbf{d^p})}dt. \tag{28}$$

By replacing $\hat{S}(|\mathbf{d^p}|, \mathbf{P})$ with Eq. (24), Eq. (21) results in:

$$\sigma_y = k\hat{\sigma}_f(\bar{\epsilon}^p)\hat{C}_C(|\mathbf{d^p}|). \tag{29}$$

By denoting, $(\sigma_y/\hat{\sigma}_f(\bar{\epsilon}^p)) = y$ and $|\mathbf{d^p}| = \dot{\gamma}^{\mathbf{p}} = \mathbf{x}$, one gets,

$$\frac{y}{k} = \hat{C}_C(x),$$
$$\text{or} \quad x = (\hat{C}_C)^{-1}(y/k). \tag{30}$$

For compressive loading, x versus y data given by Carney et al. (2006) is tabulated in Table 1. On using this experimental data, for $k = 1$ (compressive loading), one obtains by curve fitting that:

Table 1
Strain rate sensitivity of ice (Carney et al., 2006).

Strain rate ($x(s^{-1})$)	Stress scale factor (y)
1.0	1.00000
10.0	1.25660
100.0	1.51320
200.0	1.59044
300.0	1.63562
400.0	1.66768
500.0	1.69255
600.0	1.71287
700.0	1.73005
800.0	1.74493
900.0	1.75805
1000.0	1.76979
1100.0	1.78042
1500.0	1.81498
10000.0	2.02639

$$y = 0.1114\log(x) + 1, \tag{31}$$

Introducing a new constant $C = 0.1114$ for conciseness of the expressions, one finally gets,

$$x = e^{-1/C}e^{y/C}. \tag{32}$$

Introducing another constant as, $\dot{\gamma}_0 = e^{-1/C}$, and substituting the expressions for x and y, one obtains,

$$\dot{\gamma}^p = \dot{\gamma}_0 e^{\sigma_y/kC\hat{\sigma}_f}. \tag{33}$$

The above equation can be used to evaluate the visco-plastic parameter with appropriate choice of k depending on the applied loading condition, as given in Eq. (25).

2.3. Brittle damage model for ice

In order to model the distributed brittle cracking phenomenon in ice projectile during impact, the damage model proposed by Camacho and Ortiz (1996) is followed. It should be mentioned here, that the proposed damage model does not incorporate the micro-structural behavior of ice (taking into account grain size and texture) which may play an important role in progressive damage in certain forms of ice, especially columnar ice (Weiss and Schulson, 2009). However for granular ice, the micro-structure is isotropic and so are the mechanical properties (Weiss and Schulson, 2009). Furthermore, as mentioned in Section 1, the constitutive models to numerically simulate the behavior of ice are scarce in the literature. The damage model used by Carney et al. (2006) does not incorporate a progressive damage evolution law. By contrast, the present study is aimed at formulating a progressive isotropic damage evolution law in the form of distributed cracking within ice. The incorporation of micro-structural features would involve representation of the polycrystalline nature of ice within a continuum framework (see for example Roters et al. (2010)) which can be taken up in subsequent studies. The damage model proposed by Camacho and Ortiz (1996) represents nearly co-planar radial microcracks with the help of continuum damage mechanics principles to simulate the weakening effect of the material. They assumed that Hooke's law is valid for the uncracked matrix and the stress–strain relation is given as:

$$\sigma^{\mathbf{eff}} = \mathbf{C} : \epsilon^{\mathbf{eff}}. \tag{34}$$

By considering the hypothesis of elastic energy equivalence, the constitutive relation in terms of the aggregate stress and strain is given as,

$$\sigma = (\mathbf{1} - \chi)^2\mathbf{C} : \epsilon, \tag{35}$$

where, $\chi(0 < \chi < 1)$ is a scalar damage variable representing the area fraction of micro-cracks. By applying Griffith's theory of brittle fracture, the driving force for crack initiation is given by,

$$J = -\frac{\partial W(\epsilon,\chi)}{\partial \chi} - \frac{G_c}{l}, \tag{36}$$

where l is a material property, representing the spacing between micro-cracks and G_c is the fracture energy. In order to determine l, one needs to do a material-specific micro-mechanical analysis.

The above Eq. (36) for crack driving force can be derived as follows. Consider a representative volume element (RVE) as shown in Fig. 2 with a cross-sectional area of A, in which cracked area is measured as A_c. By the definition of fracture energy, G_c is the strain energy released per unit extension of the crack area, A_c so that:

$$G_c = -\frac{\partial W}{\partial A_c}, \tag{37}$$

where W is the total strain energy of the RVE and is given by $W = wV$, with w being the strain energy density and $V = Al$ the volume of the RVE. On using the chain rule of differentiation, Eq. (37) can be written as,

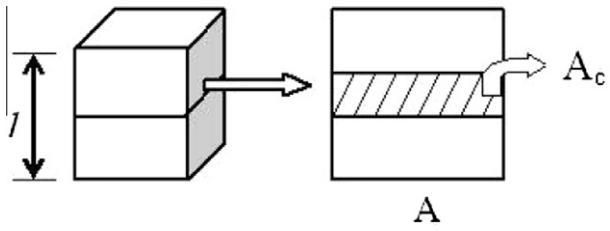

Fig. 2. Schematic of three dimensional representative volume element (RVE) with l representing spacing between micro-crack planes, A the cross sectional area of the RVE and A_C the crack area.

$$G_c = -Al\frac{\partial w}{\partial \chi}\frac{\partial \chi}{\partial A_c}. \tag{38}$$

Further, from the definition of damage variable $\chi = A_c/A$ one gets, $\partial\chi/\partial A_c = 1/A$.

On substituting this into Eq. (38), the condition for crack initiation is obtained as,

$$\frac{G_c}{l} = -\frac{\partial w}{\partial \chi}. \tag{39}$$

Thus for continued crack extension,

$$J = -\frac{\partial w}{\partial \chi} - \frac{G_c}{l} \geqslant 0. \tag{40}$$

A simple kinetic evolution equation for damage variable χ is given in terms of the crack driving force by,

$$\dot{\chi} = \frac{J}{B} \geqslant 0, \tag{41}$$

where B is a kinetic co-efficient. By letting $B \to 0$ the rate independent limit may be attained.

In this work, the above damage model is modified for ice by incorporating the effect of plasticity along with elastic degradation, within a finite deformation framework. The following assumptions are made for this purpose.

1. The laws of plasticity are written in terms of the aggregate stresses and strains (not based on matrix stresses and strains).
2. The elastic energy density is decomposed into volumetric and deviatoric part as mentioned in Section 2.1.
3. Volume of the RVE does not change due to damage, volumetric energy density will remain unaffected due to damage.

In the above derivation, volume V of the RVE is assumed as independent of χ. Such an assumption is justified as long as the cracks do not blunt significantly as χ increases. The volume change (i.e., dilatation) due to progressive damage evolution is only important in voided aggregates wherein the relevant damage variable χ would be the volume fraction of voids. Hence change in volume of the RVE during cracking induced damage in ice can be neglected given its brittle nature under high strain rate loading. Based on the above assumptions, the elastic energy density for the damaged material can be expressed as:

$$\psi_e^D = U(J^e) + (1-\chi)^2\overline{W}(\bar{\mathbf{b}}^{\mathbf{e}}). \tag{42}$$

A similar modification has to be made for plastic potential of the damaged material as:

$$\psi_p^D = (1-\chi)^2\psi_p^0(\bar{\epsilon}^p), \tag{43}$$

where, the plastic potential for the uncracked material, obeying linear hardening law is given by,

$$\psi_p^0(\bar{\epsilon}^p) = \sigma_0\bar{\epsilon}^p + \frac{h}{2}(\bar{\epsilon}^p)^2. \tag{44}$$

For an elastic–plastic material, the critical condition for crack or damage initiation is given as:

$$J = -\frac{\partial\psi}{\partial\chi} - \frac{G_c}{l} \geqslant 0, \tag{45}$$

where ψ is the total potential given by,

$$\psi = \psi_e^D + \psi_p^D. \tag{46}$$

The elastic response of the damaged material can now be expressed by modifying the deviatoric part of Kirchhoff stress as:

$$(\bar{\tau}')^{\mathbf{D}} = \mu(\mathbf{1}-\chi)^{\mathbf{2}}\mathrm{dev}(\bar{\mathbf{b}}^{\mathbf{e}}). \tag{47}$$

In the above equations, the superscript D is used to denote the damaged counterparts of the respective quantity. Since the volumetric part of the energy density remains unchanged due to damage, the hydrostatic part of Cauchy stress σ will be given by Eq. (15) (see Section 2.1). Hence, in the present approach, to determine the constitutive response of the damaged ice, only the deviatoric part of the stress component has to modified to incorporate the material degradation. The scalar damage parameter (χ) is to be treated as an internal variable and its evolution has to be obtained using Eq. (41). In order to simulate the observed dependence of failure stress on the state of stress (i.e., tension or compression) the value of G_c/l is chosen to be much smaller when the hydrostatic stress is tensile as explained in Section 4. The results of this choice are illustrated in the following examples through simulations of failure under uniaxial tension and compression. In the following section, a summary of the stress update algorithm for the constitutive model is presented.

3. Summary of explicit stress update algorithm for the constitutive model

In this section, a simple explicit (forward Euler) algorithm for updating the stresses and internal variables is described which is used along with the well known central difference method (Zienkiewicz and Taylor, 1991).

- Known at time t_n : $\mathbf{F_n}$, $\mathbf{F^e_n}$, $\mathbf{F^p_n}$, $\bar{\sigma}_\mathbf{n}$, $\sigma'_\mathbf{n}$, $\dot{\gamma}^\mathbf{p}_\mathbf{n}$
  Given at time t_{n+1} : $\mathbf{F_{n+1}}$
- Using explicit forward Euler approach, the plastic flow rule Eq. (17) is integrated as:

$$\bar{\mathbf{F}}^\mathbf{p}_{\mathbf{n+1}} = \mathbf{F}^\mathbf{p}_\mathbf{n} + \mathbf{F}^{\mathbf{e}-\mathbf{1}}_\mathbf{n}\left(\dot{\gamma}^\mathbf{p}_\mathbf{n}\frac{\mathbf{3}}{\mathbf{2}}\frac{\sigma'_\mathbf{n}}{\bar{\sigma}_\mathbf{n}}\right)\mathbf{F_n}\Delta\mathbf{t}. \tag{48}$$

and

$$\mathbf{F}^\mathbf{p}_{\mathbf{n+1}} = \left(\det\bar{\mathbf{F}}^\mathbf{p}_{\mathbf{n+1}}\right)^{-\mathbf{1/3}}\bar{\mathbf{F}}^\mathbf{p}_{\mathbf{n+1}}. \tag{49}$$

- With $\mathbf{F^p_{n+1}}$ obtained from the last step, $\mathbf{F^e_{n+1}}$ is determined as,

$$\mathbf{F}^\mathbf{e}_{\mathbf{n+1}} = \mathbf{F_{n+1}}\left(\mathbf{F}^\mathbf{p}_{\mathbf{n+1}}\right)^{-1}. \tag{50}$$

- Using $\mathbf{F^e_{n+1}}$, one can obtain the elastic left Cauchy–Green deformation as,

$$\mathbf{b}^\mathbf{e}_{\mathbf{n+1}} = \mathbf{F}^\mathbf{e}_{\mathbf{n+1}}\left(\mathbf{F}^\mathbf{e}_{\mathbf{n+1}}\right)^{\mathbf{T}}, \tag{51}$$

and

$$\bar{\mathbf{b}}^e_{n+1} = \left(J^\mathbf{e}_{n+1}\right)^{-2/3}\mathbf{b}^\mathbf{e}_{\mathbf{n+1}}. \tag{52}$$

- The deviatoric part of Kirchhoff stress is computed as:

$$\tau'_{\mathbf{n+1}} = \mu\mathrm{dev}(\bar{\mathbf{b}}^\mathbf{e}_{\mathbf{n+1}}). \tag{53}$$

- To update the pressure part, the equation-of-state as proposed in Section 2.1 is used as:

$$P_{n+1} = \hat{C}(\epsilon_V). \tag{54}$$

- The Kirchhoff stress and the Cauchy stress are updated subsequently as:

$$\tau_{\mathbf{n+1}} = \mathbf{J}^\mathbf{e}_{\mathbf{n+1}}\mathbf{P_{n+1}}\cdot\mathbf{1} + \tau'_{\mathbf{n+1}}, \tag{55}$$

$$\sigma_{\mathbf{n+1}} = J^{-\mathbf{1}}_{\mathbf{n+1}}\boldsymbol{\tau}_{\mathbf{n+1}}. \tag{56}$$

- The Mises equivalent stress is computed as:

$$\bar{\sigma}_{n+1} = \sqrt{\frac{3}{2}(\sigma'_{\mathbf{n+1}} : \sigma'_{\mathbf{n+1}})}, \tag{57}$$

where,

$$\sigma'_{\mathbf{n+1}} = \sigma_{\mathbf{n+1}} - \frac{\mathbf{1}}{\mathbf{3}}\mathrm{tr}(\sigma_{\mathbf{n+1}}). \tag{58}$$

- The flow stress is updated as:

$$\hat{\sigma}_{fn+1} = \sigma_0 + h\bar{\epsilon}^p_{n+1}, \tag{59}$$

where, equivalent plastic strain $\bar{\epsilon}^p_{n+1}$ is given by,

$$\bar{\epsilon}^p_{n+1} = \bar{\epsilon}^p_n + \sqrt{\frac{2}{3}(\mathbf{d}^\mathbf{p}_\mathbf{n} : \mathbf{d}^\mathbf{p}_\mathbf{n})}\Delta t. \tag{60}$$

- Finally, the visco-plastic parameter is updated using Eq. (33) as explained in Section 2.2:

$$\dot{\gamma}^p_{n+1} = \dot{\gamma}_0 \cdot e^{\frac{\bar{\sigma}_{n+1}}{k\bar{C}\hat{\sigma}_{fn+1}}}. \tag{61}$$

To incorporate the proposed brittle damage model the above update algorithm is modified as follows:

- The entire plastic update will remain same, as per the assumption stated in Section 2.3.
- In elastic stress update, the deviatoric stress has to be computed as:

$$(\tau'^D)_{n+1} = \mu(1-\chi_n)^2\mathrm{dev}(\bar{\mathbf{b}}^e_{n+1}). \tag{62}$$

- However, the pressure computation will not get modified. Hence, the total stress will now become:

$$\tau_{\mathbf{n+1}} = J^\mathbf{e}_{\mathbf{n+1}}P_{\mathbf{n+1}}\mathbf{1} + (\tau'^{\mathbf{D}})_{\mathbf{n+1}}. \tag{63}$$

- Finally, the damage variable has to be updated using:

$$\chi_{n+1} = \frac{J_n}{B}\Delta t + \chi_n. \tag{64}$$

4. Numerical examples

The constitutive model for ice explained in Section 2 is implemented in finite element code FEAP (Zienkiewicz and Taylor, 1991) by writing a user material subroutine. The finite element implementation is validated by conducting several single element tests and by studying some large size example problems. The entire finite element analysis is performed using explicit time integration scheme. First, a single 3-D eight noded brick element is considered under uniaxial and biaxial loading conditions, and the material input parameters are taken to be exactly same as those used by Carney et al. (2006) in their finite element simulation. The important parameters reported in Carney et al. (2006) are listed in Table 2. The yield stress in tension and compression are chosen to be very large to suppress yielding, since it has been established that failure of ice under high strain rate or impact

Table 2
Material properties corresponding to the ice constitutive model used in the simulations.

Density (ρ)	897.6 kg/m^3
Young's modulus (E)	9.31 GPa
Initial compressive flow stress	172.4 MPa
Initial tensile flow stress	17.24 MPa
Plastic tangent modulus (h)	6.89 MPa
Poisson's ratio (ν)	0.33
Pressure cut-off in compression (P_C)	4.93 MPa
Pressure cut-off in tension (P_T)	0.433 MPa
G_c/l in compression	0.01 N/mm^2
G_c/l in tension	2e−4 N/mm^2

loading occurs in a brittle manner. In order to incorporate the brittle damage model for ice as proposed in Section 2.3, three additional parameters, viz., the fracture energy (G_c), the distance between the micro-flaws (l) which can cause final failure, and the kinetic coefficient B, are needed. From published experimental data (Mulmule and Dempsey, 2000; Petrovic, 2003) for the critical stress intensity factor under mode I ($K_{Ic} = 100\ \text{kPa}\sqrt{m}$) and Young's modulus $E = 9.31$ GPa, the value of the fracture energy $G_c \approx 10^{-3}$ N/mm. By assuming the value of $l = 5$ mm, G_c/l under tensile loading is taken as 2×10^{-4} N/mm^2. When hydrostatic stress is compressive, but with unequal principal stresses, inclined cracks can initiate under mode II loading. However these planes would experience compressive normal stress. Under such a condition, crack face closure and sliding is likely to occur which will retard crack initiation. So G_c is expected to be much higher than under mode I when crack faces remain open. Thus, it is seen from experimental data that failure stress in compression is approximately seven times higher than the failure stress in tension under quasi-static loading. This implies that G_c should be approximately 50 times larger (as K_c is proportional to failure stress and G_c is proportional to K_c^2). Hence G_c/l in compression is taken as 0.01 N/mm^2.

In order to obtain the rate independent limit of the damage evolution law, a parametric study is performed by considering three values of B : $[1 \times 10^{-6}, 1 \times 10^{-7}, 1 \times 10^{-8}]$ Ns/mm^2 under quasi-static loading ($r = 0.001$/s). The stress–strain response for uniaxial tensile loading is shown in Fig. 3. It is observed that $B \leqslant 10^{-7}$ Ns/mm^2 predicts the rate independent response in the quasi-static limit. Similar trend is observed for compressive loading case also. Hence, for the subsequent analyses, the coefficient B is taken as 10^{-7} Ns/mm^2.

The tensile and compressive stress–strain behavior computed under uniaxial tensile and compressive loading are shown in Fig. 4 for the quasi-static case (10^{-3}/s). It is observed from the plot, that with the chosen input parameters, the uniaxial tensile failure stress is obtained as 1.55 MPa and the compressive failure stress as 10.3 MPa which are in reasonable agreement with the data available in literature (Petrovic, 2003). The model predicts elastic brittle failure for both types of loading. Thus, the stress–strain response is linear till the stress reaches a failure value after which it drops rapidly. This phenomenon is also observed in the available literature particularly for quasi-static loading (Dutta, 1993). Once the scalar damage parameter χ reaches a prescribed critical value of $D_c = 0.95$, the stress level attains a saturation value close to zero. A value of D_c closer to 1 used to reduce the stresses in the damaged region to small values in order to simulate loss of stress carrying capacity.

In order to study the rate effect on the stress–strain response, the uniaxial compressive and tensile loading are repeated for a range of strain rate (r) values and the results are presented in Fig. 5. Due to rate hardening behavior of ice, it is observed that the failure stress increases under high strain rate loading which corroborates with experimental observations (Schulson, 2001). Further it is also observed that the difference between the failure strength under compressive and tensile loading reduces as the strain rate increases. The compressive failure strength is approximately seven times larger than the tensile failure strength under quasi-static loading (strain rate of 10^{-3}/s), whereas the compressive failure strength is only 3.5 times larger than the tensile value at a strain rate 1/s. Thus the present numerical simulations also corroborates with the experimental observations in high strain rate case, as mentioned in Shazly et al. (2009). The compressive failure stress predicted by the model as a function of strain rate is compared with published experimental data (Jones, 1997; Kim and Keune, 2007; Meller and Cole, 1982; Shen et al., 1988) in Fig. 6. It can be seen that although the predicted failure stress is somewhat higher than the experimental data, the trend exhibited by the latter (in particular the enhancement with increasing strain rate) is well captured.

Fig. 7 shows the stress–strain response of the element subjected to hydrostatic compression. The material shows linear elastic response (see Fig. 7(a)) initially, with all the three stress components having identical variations. However, if one continues to deform the element further, the hydrostatic pressure reaches the cut-off value of −68.95 MPa (specified by the EOS, Eq. (15)) as shown in Fig. 7(b). Plastic deformation also does not occur within the

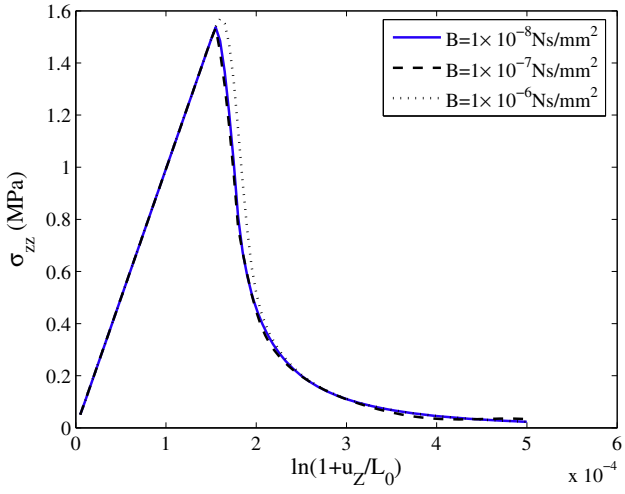

Fig. 3. Stress versus strain curves under uniaxial tension corresponding to different values of viscosity parameter B.

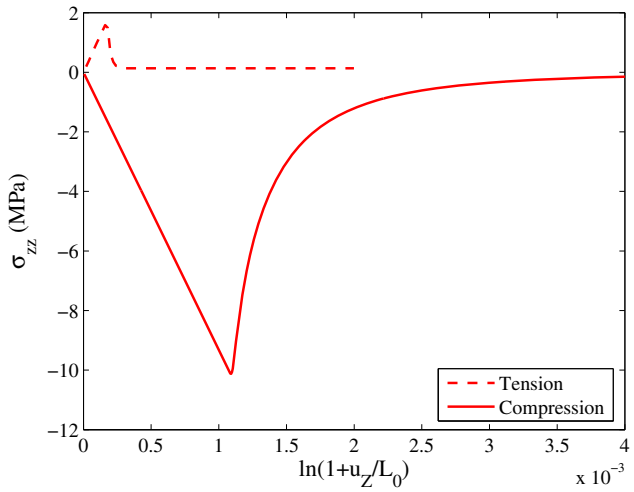

Fig. 4. Stress versus strain curve for ice in uniaxial tensile and compression loading.

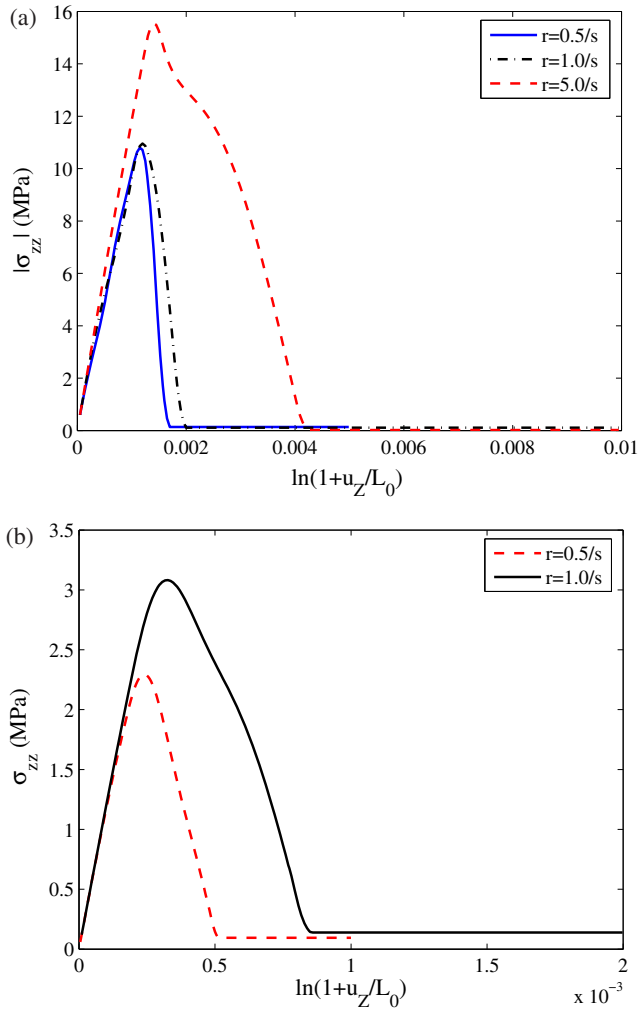

Fig. 5. Effect of strain rate on uniaxial stress–strain response under (a) compressive loading and (b) tensile loading.

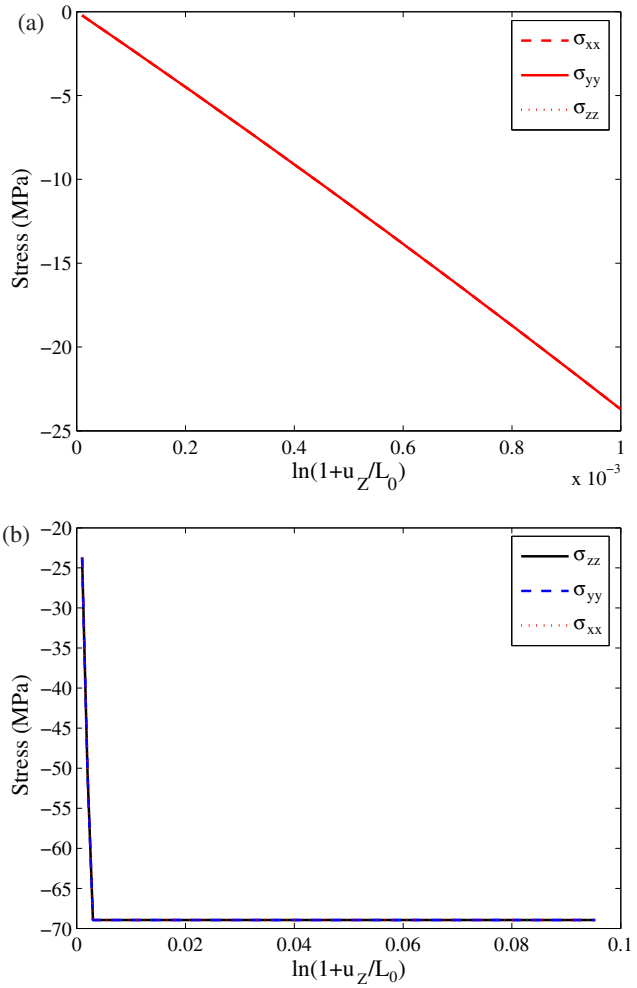

Fig. 7. Stress–strain response under compressive hydrostatic loading: (a) small strain range; (b) large strain range.

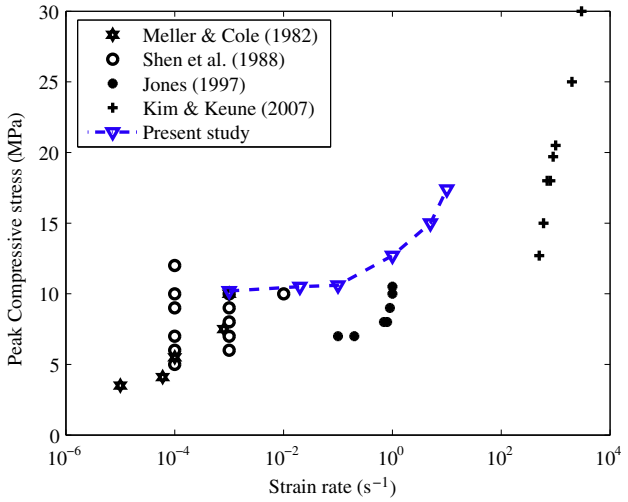

Fig. 6. Comparison between variation of compressive failure strength with strain rate predicted by the present model and published experimental data.

material, since the yield criterion used in the model is essentially based on J_2 flow theory in which plastic flow depends on the deviatoric component of the stresses only. Under such a type of loading, the failure of the material is governed by the pressure cut-off value as prescribed by the equation-of-state. Some simulations were carried out to understand the effect of lateral confining pressure on the failure strength. It was found from these simulations that confining pressure strongly enhances the tensile and compressive failure strengths. This implies that brittle cracking will be suppressed under application of confining pressure which agrees with experimental observations (Schulson, 2001).

The failure envelopes for tensile and compressive stress states are obtained numerically by modeling biaxial loading conditions. The single 3-D element is subjected to either extension or contraction in both X and Y directions. By changing the applied displacement ratio (u_x/u_y), different degrees of biaxiality can be achieved. Fig. 8(a) shows the failure envelope in stress plane obtained for compressive stress state under a strain rate of 10^{-2}/s. In this plot, the numerically obtained data are compared with the experimental results reported by Schulson (2001). There is a reasonable agreement between the two sets of data. Similarly in Fig. 8(b), the numerically simulated failure envelope is stress plane is plotted for the tensile regime. However, no experimental data is available for this stress state in order to make a comparison.

5. Simulations of failure in three-point bend bar

In order to assess the numerical capability of the proposed constitutive model for ice, few more simulations are performed

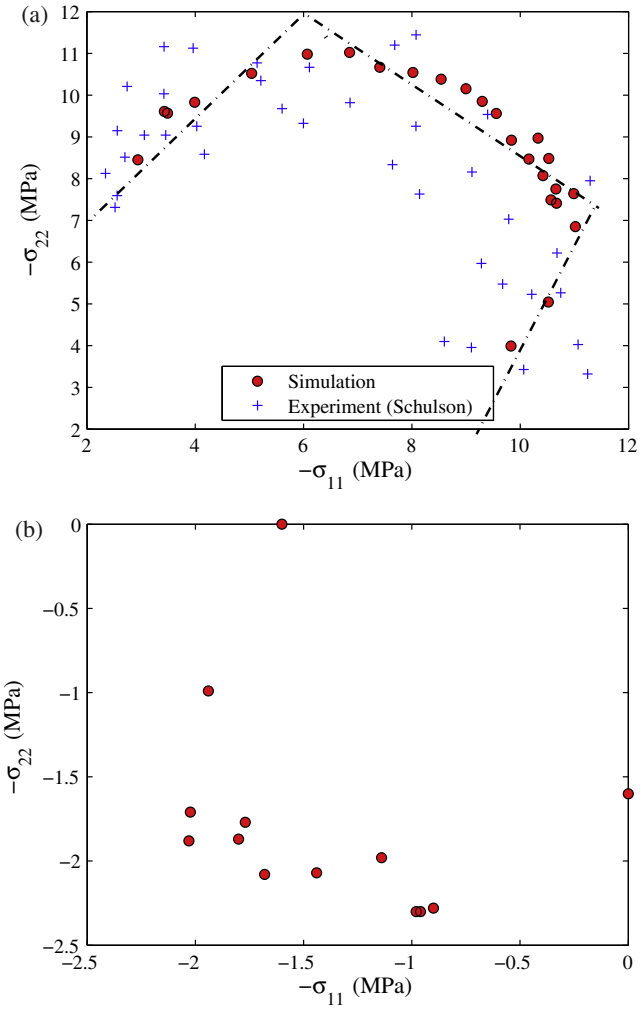

Fig. 8. Failure envelope under biaxial loading in stress plane for (a) compressive stress state and (b) tensile stress state.

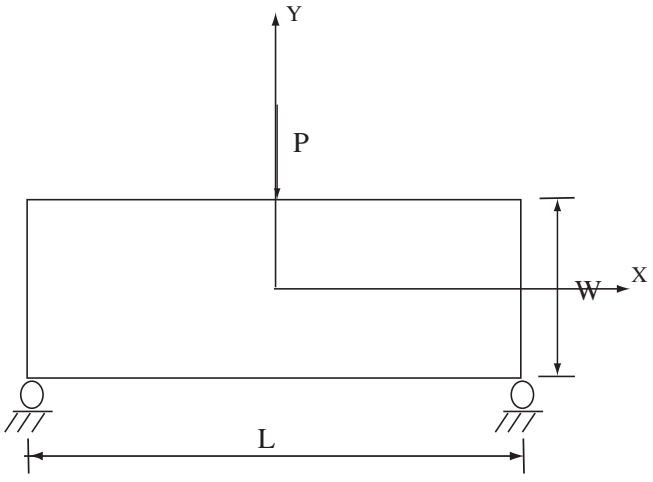

Fig. 9. Schematic diagram of the TPB (un-notched) specimen.

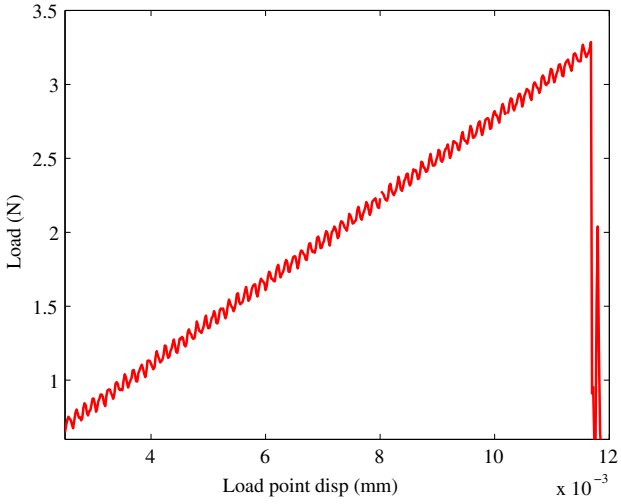

Fig. 10. Load–displacement curve of the TPB (un-notched) specimen.

involving un-notched and notched three-point bend specimens in this section.

5.1. Three point bend (un-notched) specimen

Fig. 9 shows a schematic diagram of the specimen used in the analysis. The specimen has a length of $L = 80$ mm and width $W = 20$ mm. Due to symmetry about the mid-span of the beam, only half of the specimen is modeled. The finite element mesh for this geometry comprises of 209 four-noded quadrilateral elements. The finite element analyses are performed in a displacement-controlled mode by specifying displacement in negative Y direction on the top surface nodes near the mid-plane. In order to avoid the stress concentration due to application of a concentrated load, the displacement is applied at three adjacent nodes in a distributed manner, instead of prescribing it on a single node. Symmetry conditions ($u_x = 0$) are applied along the $x = 0$ line. The material properties used in the analysis once again correspond to ice which are summarized in Table 2. In order to simulate the quasi-static loading condition, the specimen is subjected to a displacement rate of 0.01 mm/s. The specimen is loaded subsequently up to the damage initiation and propagation.

Fig. 10 shows the load–displacement plot for this simulation. It is observed that once the damage commences, the load carrying capacity of the beam drops very sharply to zero, indicating an elastic brittle damage type of response. Fig. 11 displays the spatial distribution of the damage variable over the beam at applied displacement $u_y = 0.012$ mm. From the contour plot shown in this figure, it can be seen that damage initiation takes place in the compression zone also, simultaneously with development of tensile damage. This happens because the application of transverse load at the top surface near the mid-plane of the beam introduces stress concentration, which is high enough to trigger damage in the compressive stress regime.

5.2. Three point bend (notched) specimen

The same specimen geometry as in Section 5.1 has been chosen with a notch of diameter 0.1 mm and notch length of 10 mm at the mid-span of the bar. The mesh consists of 740 four-noded quadrilateral elements. The boundary conditions applied on the specimen are the same as the un-notched beam analyzed earlier with the additional requirement that the notch surface be free of traction. In order to understand how the damage variable evolves within the specimen under quasi static loading, the displacement is applied at a rate of 0.001 mm/s. Figs. 12 and 13 display the load-deformation response and contour plot of the damage variable χ, at displacement of 0.0008 mm respectively. Fig. 13 shows that damage initiates and progresses rapidly up to critical value of 0.8 near the notch tip, due to tensile stress concentration in this

Fig. 11. Contour plot of damage variable χ in the TPB (un-notched) specimen at applied displacement of $u_y = 0.012$ mm.

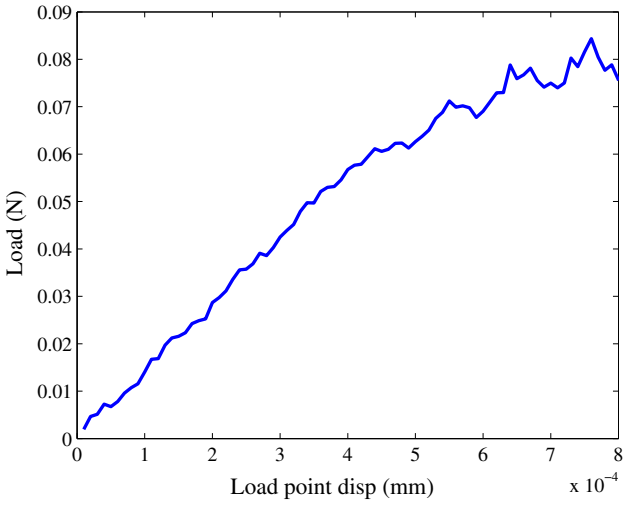

Fig. 12. Load–displacement response of TPB (notched) specimen.

Fig. 13. Contour plot of damage variable χ corresponding to centerline displacement of 0.0008 mm.

region. In this case, however, no damage occurs at the point of load application.

The non-linearity observed in the load versus displacement response is on account of development of micro-cracking induced damage near the notch tip (see Fig. 13). This also gives rise to oscillations in the load as can be noticed in Fig. 12. In brittle materials like ceramics, development of micro-cracking in the fracture process zone ahead of a notch (as seen in Fig. 13) can shield it from the far-field loading and impart some enhancement to the toughness (Anderson, 1994). However, micro-cracking is not very effective in the sense that it will not result in a rising crack growth resistance curve, which corroborates with experimental observations for brittle materials like ceramics, bulk metallic glasses and ice (Schu et al., 2007; Schulson et al., 2005). It is important to note that no attempt has been made to simulate crack extension from the notch in the present study using, say, a cohesive zone model, as in the work of Tvergaard and Hutchinson (1992). If such a simulation had been conducted, then an abrupt drop in the load–displacement curve would have occurred corresponding to the onset of unstable crack growth from the pre-existing notch.

6. Summary and conclusions

The present study was aimed at developing a constitutive model for ice, which is valid in the high strain rate or impact regime. With this objective in hand and keeping in mind the scarcity of the available models to numerically simulate the behavior of ice, the model proposed by Carney et al. (2006) has been considered as a starting basis of the present work. An equation of state has been employed which empirically represents the experimental data available for pressure versus volumetric strain behavior of ice. The occurrence of brittle damage through distributed micro-cracking has been incorporated using continuum damage mechanics principles and extended to the finite deformation regime. The proposed model has been implemented in the general purpose finite element code FEAP (Zienkiewicz and Taylor, 1991) using an explicit time integration scheme and several numerical examples have been presented to assess the performance of the model. The important conclusions from these analysis are as follows:

- The proposed continuum damage model along with chosen material parameters predicts the vast difference between tensile and compressive failure strengths of ice under quasi-static loading (with strain rate $r = 10^{-3}$/s). Thus it is found that the former is around 1.5 MPa, while the latter is about 10 MPa. These values are in good agreement with experimental results.
- The proposed model allows for continuous evolution of damage in ice due to micro-cracking. It is thermodynamically consistent and is based on continuous damage mechanics principles. This is unlike the work of Carney et al. (2006), where abrupt material failure occurs due to the damage variable being re-set to zero upon attainment of some critical conditions. Consequently, the present model is free of numerical instabilities as the damage progressively evolves in the material, which has been shown through the various examples.
- The proposed model predicts the experimentally observed increase in compressive and tensile failure strengths as function of strain rate. The ratio of the compressive to tensile strength diminishes as strain rate increases. The variation of compressive failure strength with strain rate obtained from the numerical simulations is similar to available experimental data, although it is somewhat higher.
- The failure locus in stress plane under biaxial compressive loading compares well with experimental data.
- The analysis of notched three-point bend specimen shows that micro-cracking near the notch tip may impart some toughness enhancement due to shielding which is similar to other brittle materials such as ceramics and amorphous alloys. However, the crack growth process is expected to be unstable, with little R-curve behavior since micro-cracking is not a very effective toughening mechanism.

Acknowledgement

The authors would like to gratefully acknowledge the financial support provided by Honeywell Technology Solutions Laboratory

(India) to carry out this work under a project sponsored through the Centre for Scientific and Industrial Consultancy (Indian Institute of Science).

References

Anderson, T., 1994. Fracture Mechanics: Fundamentals and Applications, second ed. CRC press.
Anghileri, M., Castelletti, L., Invernizzi, F., Mascheroni, M., 2005. A survey of numerical models for hail impact analysis using explicit finite element codes. International Journal of Impact Engineering 31, 929–944.
Armero, F., 2004. Elastoplastic and Viscoplastic Deformations in Solids and Structures. John Wiley and Sons. pp. 227–266.
Camacho, G., Ortiz, M., 1996. Computational modeling of impact damage in brittle materials. International Journal of Solids and Structures 33, 2899–2938.
Carney, K., Benson, D., Dubois, P., Lee, R., 2006. A phenomenological high strain rate model with failure for ice. International Journal of Solids and Structures 43, 7820–7839.
Carter, D., 1972. Brittle fracture of polycrystalline ice under compressive loadings. In: Proceedings of IAHR Ice Symposium, pp. 67–71.
Columbia Accident Investigation Board, 2003. Coulmbia accident investigation report. Tech. rep., NASA.
Currier, J., Schulson, E., 1982. The tensile strength of ice as a function of grain size. Acta Materialia 30, 1511–1514.
Dempsey, J., Defranco, S., Adamson, R., Mulmule, S., 1999. Scale effects on the in situ tensile strength and fracture of ice part I: large grained freshwater ice at spray lake reservoir. International Journal of Fracture 95, 325–345.
Dutta, P., 1993. Compressive failure of polycrystalline ice under impact. In: Proceedings of the 3rd International Offshore and Polar Engineering Conference. Singapore, pp. 573–580.
Dutta, P., Cole, D., Schulson, E., Sodhi, D., 2003. A fracture study of ice under high strain rate loading. In: Proceedings of the 13th International Offshore and Polar Engineering Conference. Honolulu, Hawaii, pp. 465–472.
Epifanov, V., 2005. Rupture and dynamic hardness of ice. Doklady Physics 49, 86–89.
Gold, L., 1988. On the elasticity of ice plates. Canadian Journal of Civil Engineering 19, 1080–1084.
Haynes, F., 1978. Effect of temperature on the strength of snow ice. Tech. Rep. CRREL-78-27, Department of the Army, Cold Regions Research and Engineering Laboratory, Hanover, New Hampshire.
Jones, S., 1997. High strain rate compression tests on ice. Journal of Physical Chemistry 32, 6099–6101.
Kim, H., Kedward, K., 2000. Modeling hail ice impacts and predicting impact damage initiation in composite structures. AIAA Journal 38, 1278–1288.
Kim, H., Keune, J., 2007. Compressive strength of ice at impact strain rates. Journal of Material Science 42, 2802–2806.
Lee, E., 1969. Elastic plastic deformation at finite strains. Journal of Applied Mechanics 36, 1–6.
Lubliner, J., 1990. Plasticity Theory. Macmillan, New York, USA.
Mandel, J., 1973. Plasticite classique et viscoplasticite. International Journal of Solids and Structures 9, 725–740.
Mcnaughtan, I., Chisman, S., 1969. A study of hail impact at high speed on light alloy plates. In: 9th Annual National Conference on Environmental Effects on Aircraft and Propulsion System.
Meller, M., Cole, D., 1982. Deformation and failure of ice under constant stress or constant strain rate. Cold Regions Science and Technology 5, 201–219.
Mulmule, S., Dempsey, J., 2000. LEFM size requirements for the fracture testing of ice. IJF 102, 85–98.
Pereira, J., Padula, S., Revilock, D., Melis, M., 2006. Forces generated by high velocity impact of ice on a rigid structure. Tech. Rep. TM-2006-214263, NASA.
Petrovic, J., 2003. A review on mechanical properties of ice and snow. Journal of Material Science 38, 1–6.
Roters, F., Eisenlohr, P., Hantcherli, L., Tjahjanto, D., Bieler, T., Raabe, D., 2010. Overview of constitutive laws, kinematics, homogenization and multiscale methods in crystal plasticity finite-element modeling: theory, experiments, applications. Acta Materialia 58, 1152–1211.
Schu, C., Hufnagel, T., Ramamurthy, U., 2007. Mechanical behavior of amorphous alloys. Acta Materialia 55, 4067–4109.
Schulson, E., 2001. Brittle failure of ice. Engineering Fracture Mechanics 68, 1839–1887.
Schulson, E., LLiescu, D., Frott, A., 2005. Characterization of ice for return-to-flight of the space shuttle. Part 1-Hard Ice. Tech. Rep. NASA CR-2005-213643, NASA.
Shazly, M., Prakash, V., Lerch, B., 2005. High strain rate compression testing of ice. Tech. Rep. TM-2005-213966, NASA.
Shazly, M., Prakash, V., Lerch, B., 2009. High strain-rate behavior of ice under uniaxial compression. International Journal of Solids and Structures 46, 1499–1515.
Shen, L., Zhao, S., Lu, X., Shi, Y., 1988. In: Proceedings of the Seventh International Conference on Offshore Mechanics and Arctic Engineering. ASME, NewYork, pp. 19–23.
Sherburn, J., Horstemeyer, M., 2010. Hydrodynamic modeling of impact craters in ice. International Journal of Impact Engineering 37, 27–36.
Simo, J., 1988. A framework for finite strain elastoplasticity based on maximum plastic dissipation and the multiplicative decomposition. Part II: computational aspects. Computer Methods in Applied Mechanics and Engineering 68, 1–31.
Simo, J., Hughes, T., 1996. Computational Inelasticity. Springer Verlag.
Tvergaard, V., Hutchinson, J., 1992. The relation between crack growth resistance and fracture process parameters in elastic plastic solids. JMPS 40, 1377–1397.
Weiss, J., Schulson, E., 2009. Coulombic faulting from the grain scale to the geophysical scale. Journal of Physics D: Applied Physics 42, 214017–214035.
Zienkiewicz, O., Taylor, R., 1991. The Finite Element Method, fifth ed.. Basic Formulation and Linear Problems Mc-Graw-Hill, London. p. 1.